N-body simulations of the Self–Confinement of Viscous Self–Gravitating Narrow Eccentric Planetary Ringlets

Joseph M. Hahn,[1] Douglas P. Hamilton,[2] Thomas Rimlinger,[2] and Lucy Luu[2]

[1]*Space Science Institute*
[2]*University of Maryland*

ABSTRACT

N-body simulations are used to illustrate how narrow eccentric planetary ringlets can evolve into a self–confining state.

1. INTRODUCTION

Narrow eccentric planetary ringlets have properties both interesting and not well understood: sharp edges, sizable eccentricity gradients, and a confinement mechanism that opposes radial spreading due to ring viscosity. Prevailing ringlet confinement mechanisms include: unseen shepherd satellites (reference), periapse pinch (ref), self gravity (ref), and self-confinement (ref). This study uses N-body simulations to show how a viscous narrow self–gravitating ringlet can evolve into a self-confining state.

2. RINGLET CONFINEMENT MECHANISMS

This section will explain the pros and cons of the various ringlet confinement mechanisms, and will then motivate the possibility that ringlets are self confining. That possibility is explored further via numerical simulations using the epi_int_lite N-body integrator.

3. EPI_INT_LITE

Epi_int_lite is a child of the epi_int N-body integrator that was used to simulate the outer edge of Saturn's B ring while it is sculpted by satellite perturbations (Hahn & Spitale 2013). The new code is very similar to its parent but differs in two significant ways: (*i.*) epi_int_lite is written in python and recoded for more efficient execution, and (*ii.*) epi_int_lite uses a more reliable drift step to handle unperturbed motion around an oblate planet (detailed in Appendix A).

Otherwise epi_int_lite's treatment of ring self–gravity and viscosity are identical to that used by the parent code; see Hahn & Spitale (2013) for additional details. The epi_int_lite source code is available

Corresponding author: Joseph M. Hahn
jhahn@spacescience.org

at https://github.com/joehahn/epi_int_lite, and the code's numerical quality is assessed in Appendix B where the output of several numerical experiments are compared against theoretical expectations.

Calculations by epi_int_lite use natural units with gravitation constant $G = 1$, central primary mass $M = 1$, and the ringlet's inner edge has initial radius $r_0 = 1$, and so the ringlet masses m_r and radii r quoted below are in units of M and r_0. Converting code output from natural units to physical units requires choosing physical values for M and r_0 and multiplying accordingly, and when this text does so it assumes Saturn's mass $M = 5.68 \times 10^{29}$ gm and a characteristic ring radius $r_0 = 1.0 \times 10^{10}$ cm. Simulation time t is in units of $T_{\mathrm{orb}}/2\pi$ where $T_{\mathrm{orb}} = 2\pi\sqrt{r_0^3/GM}$ is the orbit period at r_0, so divide simulation time t by 2π and multiply by T_{orb} to convert simulation time from natural to physical units. The simulated particles' motions during the drift step are also sensitive to the J_2 portion of the primary's non-spherical gravity component (see Appendix B), and all simulations adopt Saturn-like values of $J_2 = 0.01$ and $R_p = r_0/2$ where R_p is the planet's mean radius.

3.1. *streamlines*

Initially all particles are assigned to various streamlines across the simulated ringlet. A streamline is a closed eccentric path around the primary, and each streamline is populated by N_p particles that are initially assigned a common semimajor axis a and eccentricity e while distributed uniformly in longitude. Most of the simulations described below employ only $N_s = 2$ streamlines, so that the model output can be benchmarked against theoretical treatments that also treat the ringlet as two gravitating rings (e.g. Borderies et al. 1983). But the following also performs a few higher-resolution simulations using $N_s = 11$ streamlines, to demonstrate that the $N_s = 2$ treatment is perfectly adequate and reproduces all the relevant dynamics. All simulations use $N_p = 241$ particles per streamline, and the total number of particles is $N_s N_p$. Note that the assignment of particles to a given streamline is merely for labeling purposes, as particles are still free to wander in response to the ring's internal forces, namely, ring gravity and viscosity. But as Hahn & Spitale (2013) as well as this work shows, the simulated ring stays coherent and highly organized throughout the simulation such that particles on the same streamline do not pass each other longitudinally, nor do they cross adjacent streamlines. Because the simulated ringlet stays highly organized, there is no radial or longitudinal mixing of the ring particles, and simulated particles preserve their streamline membership over time.

3.2. *N-body method*

The epi_int_lite N-body integrator uses the same drift-kick scheme used by the MERCURY Nbody algorithm (Chambers 1999) except that epi_int_lite particles that do not interact with each other directly. Rather, epi_int_lite particles are only perturbed by the accelerations exerted by the ringlet's individual streamlines. Those accelerations are sensitive to the streamline's relative separations and velocities, which are inferred from the particles' positions and velocities. Epi_int_lite particles are thus trace particles that indicate the streamlines' locations and orientations, which the N-body integrator uses to compute the orbital evolution of those trace particles due to the perturbations exerted by those streamlines. This streamline approach is widely used in theoretical studies of planetary rings (c.f. Goldreich & Tremaine 1979; Borderies et al. 1983, 1985) as well as in N-body studies of rings (Hahn & Spitale 2013; Rimlinger et al. 2016). The great benefit of the streamline concept in numerical work is that it allows one to swiftly track the global evolution of the ringlet's streamlines numerically using only a modest numbers of trace particles, typically $N_s N_p \sim 500$.

The simulations reported on here account for streamline gravity and ringlet viscosity. Because a ringlet is narrow, all particles are in close proximity to the nearby portions of all streamlines, which allows us to approximate a streamline as an infinitely long wire of matter having linear density λ. Consequently the gravity of each perturbing streamline draws a particle towards that streamline with acceleration

$$A_g = \frac{2G\lambda}{\Delta},$$ (1)

where Δ is the particle's distance from the streamline.

The hydrodynamic approximation is used here to account for the dissipation that occurs as particles in adjacent particle streamlines shear past and collide with the perturbed particle, without having to monitor individual particle-particle collisions. The particle's acceleration due to the ring particles' shear viscosity is

$$A_{\nu,\parallel} = -\frac{1}{\sigma r}\frac{\partial \mathcal{F}_L}{\partial r},$$ (2)

where r is the particle's radial coordinate, σ is the surface density of ringlet matter, and $\mathcal{F}_{L,\nu}$ is the flux of angular momentum that is transported radially across the particle's streamline due to its collisions with particles in adjacent streamlines, *i.e.*

$$\mathcal{F}_{L,\nu} = -\nu_s \sigma r^2 \frac{\partial \omega}{\partial r}$$ (3)

where ν_s is the ringlet's kinematic shear viscosity and $\omega = v_\theta / r$ is the particle's angular velocity (Hahn & Spitale 2013). The acceleration $A_{\nu,\parallel}$ is parallel to the perturbed particle's streamline *i.e.* parallel to particle's velocity vector $\mathbf{v} = \dot{\mathbf{r}} = v_r \hat{r} + v_\theta \hat{\theta}$ where $\mathbf{r} = r\hat{r}$ is the particle's position vector.

Dissipative collisions also transmits linear momentum in the perpendicular direction, which results in the additional acceleration

$$A_{\nu,\perp} = -\frac{1}{\sigma}\frac{\partial \mathcal{G}}{\partial r}$$ (4)

where the radial flux of linear momentum due to ringlet viscosity is

$$\mathcal{G} = -\left(\frac{4}{3}\nu_s + \nu_b\right)\sigma\frac{\partial v_r}{\partial r} - \left(\nu_b - \frac{2}{3}\nu_s\right)\frac{\sigma v_r}{r}$$ (5)

ν_b is the ringlet's kinematic bulk viscosity and v_r is the paricle's radial velocity (Hahn & Spitale 2013).

In the hydrodynamic approximation there is also the acceleration due to ringlet pressure p that is due to particle-particle collisions,

$$A_p = -\frac{1}{\sigma}\frac{\partial p}{\partial r}.$$ (6)

Epi_int_lite treats the particle ring as a dilute gas of colliding particles for which the 1D pressure is $p = c^2\sigma$ where c is the particles dispersion velocity. However Hahn & Spitale (2013) found ring pressure to be inconsequential in N-body simulations of Saturn's A ring, and the ringlet simulation described in Section (???) also shows no sensitivity to pressure effects, so all other simulations reported on here have $c = 0$.

4. N-BODY SIMULATIONS OF VISCOUS GRAVITATING RINGLETS

The folowing describes a suite of N-body simulations of narrow viscous gravitating planetary ringlets, to highlight the range of initial ringlet conditions the do evolve into a self-confining state, and those that do not.

4.1. *nominal model*

Figure 1 shows the semimajor axis evolution of what is referred to as the nominal model since this ringlet readily evolves into a self-confining state. The simulated ringlet is composed of $N_s = 2$ streamlines having $N_p = 241$ particles per streamline, and the integrator timestep is $\Delta t = 0.5$ in natural units, so the integrator samples the particles' orbits $2\pi/\Delta t \simeq 13$ times per orbit, and this ringlet is evolved for 4.7×10^3 orbits, which requires 15 minutes execution time on a 5 year old laptop. The ringlet's mass is $m_r = 5 \times 10^{-10}$, its shear viscosity is $\nu_s = 2.5 \times 10^{-12}$, and its bulk viscosity is $\nu_b = \nu_s$. The ringet's initial radial width is $\Delta a_0 = 3 \times 10^{-4}$, its initial eccentricity is $e = 0.01$, and its eccentricity gradient is initially zero. A convenient measure of time is the ringlet's viscous radial spreading timescale

$$\tau_\nu = \frac{\Delta a_0^2}{12\nu_s}, \tag{7}$$

which can be inferred from Eqn. (2.13) of Pringle (1981). This simulation's viscous timescale is $\tau_\nu = 3.0 \times 10^3$ in natural units or $\tau_\nu/2\pi = 4.8 \times 10^2$ orbital periods. If this ringlet were orbiting Saturn at $r_0 = 1.0 \times 10^{10}$ cm then the simulated ringlet's physical mass would be $m_r = 2.8 \times 10^{20}$ gm which is equivalent to the mass of a 41 km radius iceball assuming a volume density $\rho = 1$ gm/cm^3, and the ringlet's initial radial width would be $\Delta a_0 = 3 \times 10^{-4} r_0 = 30$ km. This ringlet's orbit period would be $T_{orb} = 2\pi\sqrt{r_0^3/GM} = 9.0$ hours in physical units, so the ringlet's viscous timescale is $\tau_\nu = 12$ years, and so its shear viscosity is $\nu_s = \Delta a_0^2/12\tau_\nu = 4.8 \times 10^4$ cm^2/sec when evaluated in physical units. This ringlet's initial surface density would be $\sigma = m_r/2\pi r_0 \Delta a_0 = 1500$ gm/cm^2, but Figs. 1–2 show that shrinks by a factor of 4 as the ringlet's sememajor axis width Δa grows via viscous spreading until it settles into the self-confining state at time $t \sim 20\tau_\nu$. This so-called nominal ringlet is probably overdense and overly viscous compared to known planetary ringlets, but that is by design so that the simulated ringlet quickly settles into the self-confining state. Section XX also shows how outcomes scale when a wide variety of alternate initial masses, orbits, and viscosities are also considered.

Figure 3 shows that the outer streamline's eccentricity initially grows at the expense of the inner streamline's, and this is a consequence the self-gravitating ringlet's secular perturbations of itself, which is also demonstrated in Appendix C. Figure 4 shows the ringlet's eccentricity difference $\Delta e = e_{\text{outer}} - e_{\text{inner}}$ and longitude of periapse difference $\Delta\tilde{\omega} = \tilde{\omega}_{\text{outer}} - \tilde{\omega}_{\text{inner}}$, which both settle into equilibrium values after the ringlet arrives at the self-confining state.

Figure 5 shows the radii of the ringlet's two streamlines plotted versus their relative longitude $\varphi = \theta - \tilde{\omega}_{\text{inner}}$ at time $t = 100\tau_\nu$ when the simulation ends. In all simulations examined here, the ringlet's periapse twist $\Delta\tilde{\omega} = \tilde{\omega}_{\text{outer}} - \tilde{\omega}_{\text{inner}}$ is negative, so the outer streamline's longitude of periapse $\tilde{\omega}$ trails the inner streamline's, which in turn causes the streamlines' separations along the ringlet's pre-periapse side (where $\varphi < 0$) to be smaller than at post-periapse ($\varphi > 0$). Which makes the ringlet's surface density asymmetric, with maximum surface density occurring just prior to periapse, see Figs. 5–7.

Figure 1. Evolution of the nominal ringlet's semimajor axes a versus time t in units of the ringlet's viscous time τ_ν. This ringlet is composed of $N_s = 2$ streamlines, and the outer (blue) and inner (green) streamlines' semimajor axes are plotted relative to their mean a_mean, and displayed in units of the ringlet's initial width $\Delta a_0 = 3 \times 10^{-4}$ in natural units (*i.e.* $G = M = r_0 = 1$). The simulated ringlet has total mass $m_r = 5 \times 10^{-10}$, shear viscosity $\nu_s = 2.5 \times 10^{-12}$, and initial eccentricity $e = 0.01$. See Section 4.1 to convert m_r, a and ν_s from natural units to physical units.

It is convenient to recast these orbit element differences as dimensionless gradients

$$e' = a\frac{de}{da} \qquad \text{and} \qquad \tilde{\omega}' = ea\frac{d\tilde{\omega}}{da} \tag{8}$$

as these are the terms that contribute to the nonlinearity parameter of Borderies et al. (1983):

$$q = \sqrt{e'^2 + \tilde{\omega}'^2}. \tag{9}$$

See also Fig. 8 which plot's the nominal ringlet's dimensionless eccentricity gradient e', dimensionless periapse twist $\tilde{\omega}'$, and nonlinearity parameter q versus time. All simulations examined here have $|\tilde{\omega}'| \ll |e'|$ so that $q \simeq |e'|$, and all simulated self-confining ringlets have a positive eccenticity gradient and a negative periapse twist such that the outer ringlet's periapse trails the inner ringlet's, consistent with the findings of Borderies et al. (1983).

5. ANGULAR MOMENTUM AND ENERGY FLUXES, AND LUMINOSITIES

The above evolution is readily understood when the ringlet's radial flux of angular momentum and energy are considered.
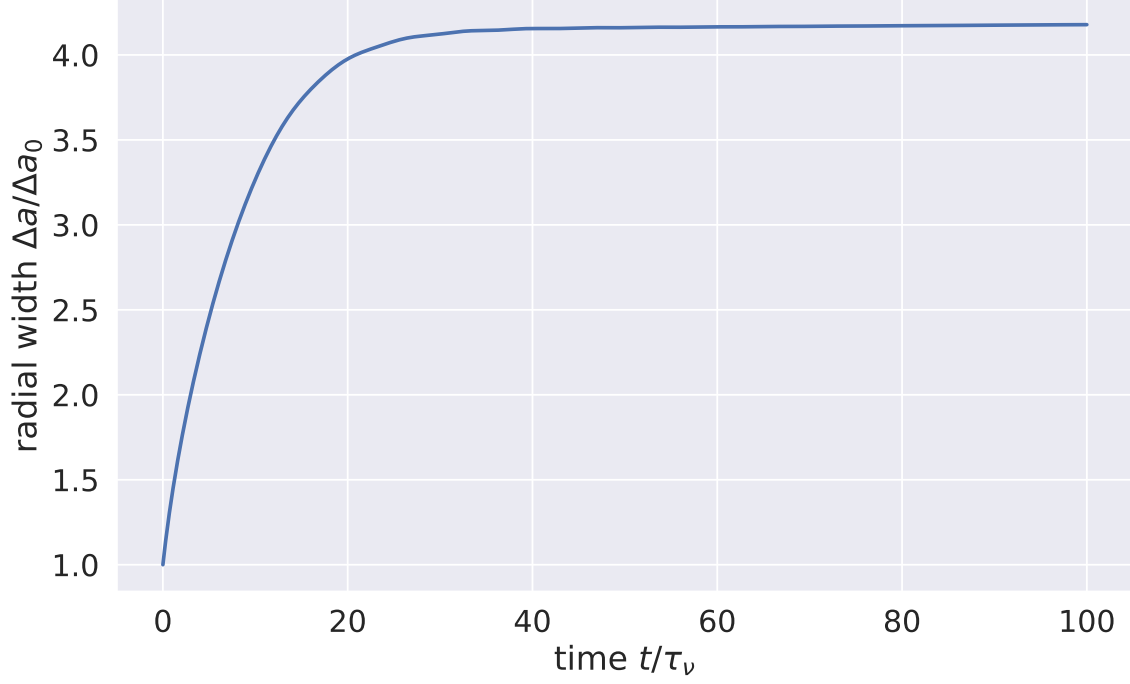
Figure 2. The nominal ringlet's semimajor axis width $\Delta a = a_{\mathrm{outer}} - a_{\mathrm{inner}}$ over time and in units of its initial radial width Δa_0.
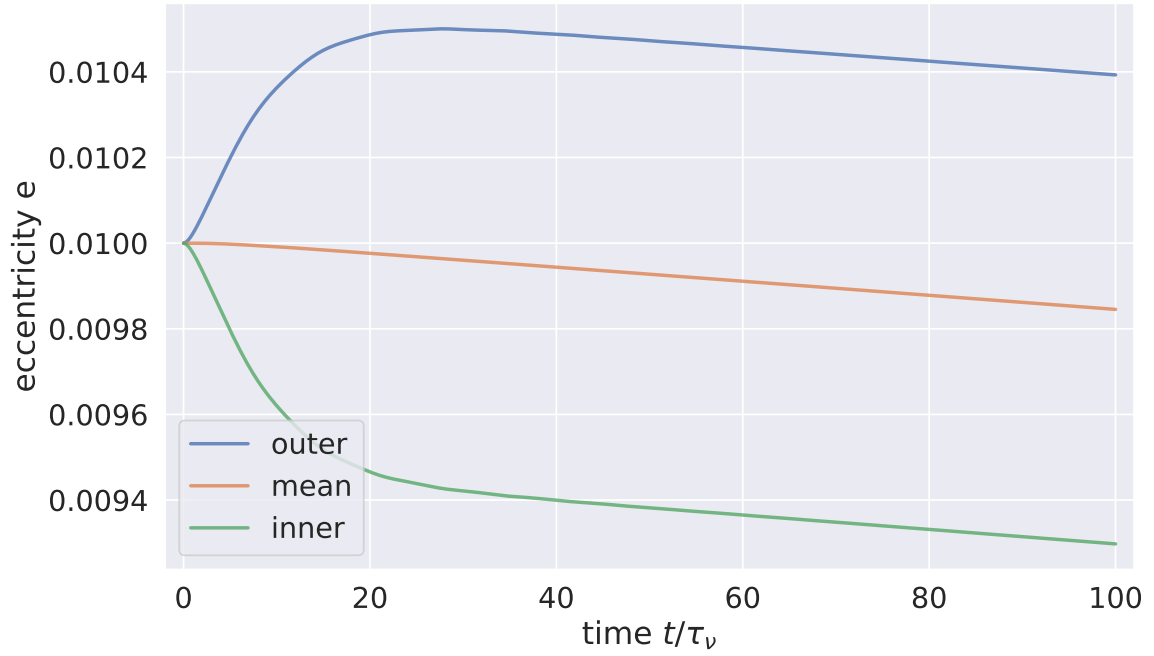

Figure 3. The nominal ringlet's eccentricity evolution.

Figure 4. The nominal ringlet's eccentricity difference $\Delta e = e_{\text{outer}} - e_{\text{inner}}$ and longitude of periapse difference $\Delta\tilde{\omega} = \tilde{\omega}_{\text{outer}} - \tilde{\omega}_{\text{inner}}$ in radians divided by 10.

Figure 5. The radii of the nominal ringlet's streamlines are plotted versus relative longitude $\varphi = \theta - \tilde{\omega}$ at time $t = 100\tau_\nu$, with Δa being the streamlines' semimajor axis difference then. Inset plot shows outer streamline's longitude of periapse $\tilde{\omega}$ trailing the inner streamline's.

surface density vs longitude

Figure 6. Nominal ringlet's surface density $\sigma(\varphi)$ versus relative longitude φ at selected times t and plotted in units of ringlet's initial mean surface density σ_0. Note that the ringlet's surface density maxima occurs just before peripase, and is due to the ringlet's negative periapse twist $\Delta\tilde\omega = \tilde\omega_{\mathrm{outer}} - \tilde\omega_{\mathrm{inner}} < 0$.

5.1. angular momentum and energy fluxes

The torque that is exerted on a small streamline segment of mass δm at location $\mathbf{r} = r\hat{\mathbf{r}}$ due to the streamlines orbiting interior to it is $\delta T = \delta m \mathbf{r} \times \mathbf{A}^1$ where $\mathbf{A}^1 = A_r^1\hat{\mathbf{r}} + A_\theta^1\hat{\boldsymbol{\theta}}$ is the so-called one-sided acceleration that is exerted on δm by the interior streamlines. Since $\delta m = \lambda\delta\ell$ where λ is the streamline's linear mass density, and $\delta\ell$ is the segment's length, then the radial flux of angular momentum flowing into that segment due to the accelerations that are exerted by streamlines orbiting interior to that segment is

$$\mathcal{F}_L(r,\theta) = \frac{\delta T}{\delta\ell} = \lambda r A_\theta^1, \tag{10}$$

where A_θ^1 is the tangential component of the one-sided acceleration. A streamline of semimajor axis a in a ringlet having total mass m_r distributed across N_s streamlines will have a linear mass density $\lambda = m_r/N_s/2\pi a$. The radial angular momentum flux, Eqn. (10), is due to the ringlet's viscosity and self-gravity, so $\mathcal{F}_L = \mathcal{F}_{L,\nu} + \mathcal{F}_{L,g}$.

The work that the interior streamlines exert on δm as that segment travels a small distance $\delta\mathbf{r} = \mathbf{v}\delta t$ in time δt is $\delta W = \delta m \mathbf{A}^1 \cdot \delta\mathbf{r}$ where $\mathbf{v} = v_r\hat{\mathbf{r}} + v_\theta\hat{\boldsymbol{\theta}}$ is the segment's velocity, and that work accrues at δm at the rate $\delta W/\delta t = \lambda\mathbf{A}^1 \cdot \mathbf{v}\delta\ell$, so the radial flux of energy entering that ringlet segment due to accelerations exerted by the interior streamlines is

$$\mathcal{F}_E(r,\theta) = \frac{\delta W}{\delta\ell\delta t} = \lambda\mathbf{A}^1 \cdot \mathbf{v}, \tag{11}$$

and this radial energy flux is due to the ringlet's viscosity and self-gravity, $\mathcal{F}_E = \mathcal{F}_{E,\nu} + \mathcal{F}_{E,g}$.

radial surface density profiles

Figure 7. Radial profiles of the nominal ringlet's surface density $\sigma(\varphi)$ at time $t/\tau_\nu = 100$ when the ringlet is self-confining. Each surface density profile is plotted versus radial distance r relative to r_{mid}, which is the ringlet's midpoint along relative longitude $\varphi = \theta - \tilde{\omega}$, with those radial distances $r - r_{mid}$ measured in units of the ringlet's final semimajor axis width Δa, and surface density is shown in units of the ringlet's longitudinally-averaged surface density σ_0. Radial surface density profiles are plotted along the ringlet's periapse ($\varphi = 0$, blue curve), which is where the ringlet's streamlines are most concentrated and surface denisity σ is greatest due to the ringlet's eccentricity gradient e', at the pre-periapse quadrature ($\varphi = -\pi/2$, red curve), post-periapse quadrature ($\varphi = \pi/2$, green curve) and at apoapse ($|\varphi| = \pi$, orange curve) where streamlines have their greatest separation and ringlet surface density is lowest. This ringlet's surface density contrast, between periapse and apoapse, is 14.

5.2. luminosities

The streamline containing segment δm has semimajor axis a, and integrating the radial angular momentum flux $\mathcal{F}_L$ about the entire streamline then yields the radial luminosity of angular momentum entering streamline a,

$$\mathcal{L}_L(a) = \oint \mathcal{F}_L d\ell, \tag{12}$$

which is the torque that is exerted on streamline a by those orbiting interior to it. Similarly, integrating the radial energy flux $\mathcal{F}_E$ about streamline a also yields the ringlet's radial energy luminosity

$$\mathcal{L}_E(a) = \oint \mathcal{F}_E d\ell, \tag{13}$$

and this is the rate that interior streamlines communicate energy to streamline a.

5.3. viscous transport of angular momentum

Figure 8. The nominal ringlet's dimensionless eccentricity gradient $e' = a\Delta e/\Delta a$ (blue curve), dimensionless periapse twist $\tilde{\omega}' = ea\Delta\tilde{\omega}/\Delta a$ (orange), and nonlinearity parameter $q = \sqrt{e'^2 + \tilde{\omega}'^2}$ (green) versus time t/τ_ν. Dotted red line is the threshold for self-confinement in a non-gravitating ringlet, $e' = \sqrt{3}/2 \simeq 0.866$

Angular momentum is transported radially through the ring via viscosity and self-gravity, so $\mathcal{F}_L = \mathcal{F}_{L,\nu} + \mathcal{F}_{L,g}$, where the ringlet's viscous flux of angular momentum is

$$\mathcal{F}_{L,\nu}(r,\theta) = -\nu_s \sigma r^2 \frac{\partial \omega}{\partial r} \tag{14}$$

when written as a function of spatial coordinates and angular velocity $\omega = \dot{\theta}$ (Eqn. 14). If we consider a small arc of ring material oflength $d\ell$, then $\mathcal{F}_{L,\nu}d\ell$ is the torque that arc exert exerts on ring matter just exterior, due to viscous friction, so that is the rate that friction transmits angular momentum radially across that arc. And when $\mathcal{F}_{L,\nu}$ is evaluated along a single eccentric streamline of semimajor axis a, the above simplifies to

$$\mathcal{F}_{L,\nu}(a,\varphi) = \mathcal{F}_{L,\nu,c} \frac{1 - \frac{4}{3}e'\cos\varphi}{(1 - e'\cos\varphi)^2} \tag{15}$$

where $\varphi = \theta - \tilde{\omega}$ is the longitude relative to periapse and $\mathcal{F}_{L,\nu,c} = \frac{3}{2}\nu_s\sigma_0 a\Omega$ is the viscous angular momentum flux through a circular streamline of semimajor axis a and angular speed $\Omega(a)$, with Eqn. (15) assuming that $|\tilde{\omega}'| \ll e'$ so that $q \simeq e'$ (see Borderies et al. 1982 and Appendix D). Integrating the above around the streamline's circumference then yields its angular momentumum luminosity,

$$\mathcal{L}_{L,\nu}(a) = \oint \mathcal{F}_{L,\nu}(a,\varphi)rd\varphi = \mathcal{L}_{L,\nu,c} \frac{1 - \frac{4}{3}e'^2}{(1 - e'^2)^{3/2}}, \tag{16}$$

which is the torque that one streamline exerts on its exterior neighbor due to viscous friction (Borderies et al. 1982 and Appendix D), with $\mathcal{L}_{L,\nu,c} = 3\pi\nu_s\sigma_0 a^2\Omega$ being the viscous angular momentum luminosity of a circular streamline.

Borderies et al. (1982) examine angular momentum transport through a viscous eccentric but non-gravitating ringlet, and use Eqns. (15–16) to show that this transport has three regimes distinguished by the ringlet's e':

1. $e' < 3/4$. The ringlet's viscous angular momentum flux $\mathcal{F}_{L,\nu}(\varphi) > 0$ at all ringlet longitudes θ. The ringlet's viscous angular momentum luminosity $\mathcal{L}_{L,\nu} > 0$, so viscous friction transports angular momentum radially outwards, and the inner ring matter evolves to smaller orbits while exterior ring matter evolves outwards, and the ringlet spreads radially.

2. $3/4 \leq e' < \sqrt{3}/2$. In this regime there is a range of longitudes θ where the viscous angular momentum flux is reversed such that $\mathcal{F}_{L,\nu}(\varphi) < 0$. That angular momentum flux reversal is due to the $\partial\omega/\partial r$ term in Eqn. (14) changing sign near periapse when $e' > 0.75$; see Fig. 9. Nonetheless $\mathcal{L}_{L,\nu}$, which is proportional to the orbit-average of $\mathcal{F}_{L,\nu}(\varphi)$, is positive and the ringlet still spreads radially, albeit slower than when $e' < 0.75$.

3. $e' > \sqrt{3}/2$. Viscous angular momentum flux reversal is complete such that $\mathcal{L}_{L,\nu} < 0$, viscous friction transports angular momentum radially inwards, and the ringlet shrinks radially. But if $e' = \sqrt{3}/2 \simeq 0.866$ then $\mathcal{L}_{L,\nu} = 0$ and the ringlet's radial evolution ceases, and the viscous but non-gravitating ringlet is self confining.

Note though that the nominal ringlet's eccentricity gradient exceeds the $e' = \sqrt{3}/4 \simeq 0.866$ threshold (which is the dotted red line in Fig. 8) when it settles into self-confinement. This is due to the ringlet's self-gravity, which also transports a flux of angular momentum $\mathcal{F}_{L,g}$ radially through the ringlet.

Figure 10 shows the nominal ringlet's viscous angular momentum flux $\mathcal{F}_{L,\nu}$ versus relative longitude $\varphi = \theta - \tilde{\omega}$ at selected times t. Early in the ringlet's evolution when time $t \leq 8\tau_\nu$ (blue, orange, green, red, and purple curves), the ringlet is in regime 1 since $e' < 0.75$ and $\mathcal{F}_{L,\nu}(\varphi) > 0$ at all longitudes. But by time $t = 10\tau_\nu$ (brown curve), this ringlet's eccentricity gradient exceeds 0.75, and angular momentum flux reversal $\mathcal{F}_{L,\nu}(\varphi) < 0$ occurs near periapse where $|\varphi| \simeq 0$ where the ringlet is most overdense due to its eccentricity gradient, see also Fig. 7; this ringlet is in regime 2 and its radial spreading is reduced by angular momentum flux reversal. And by time $t = 20\tau_\nu$ (yellow curve), this ringlet is seemingly in regime 3 since $e' = 0.866$, so one might expect the ringlet's spreading to have stalled by now, but keep in mind that the above analysis ignores any transport of angular momentum via ringlet self–gravity. Figure 2 shows that this gravitating ringlet's spreading has ceased soon after time $t \simeq 35\tau_\nu$, at which point $e' = 0.88$ (cyan curve), angular momentum flux reversal is nearly complete, with the ringlet's total angular momentum luminosity $\mathcal{L}_L = \mathcal{L}_{L,\nu} + \mathcal{L}_{L,g}$ is very close to zero.

Figure 11 and Fig. 12 show that, when the ringlet is self-confining at times $t \gg 35\tau_\nu$, its positive viscous angular momentum luminosity $\mathcal{L}_{L,\nu} \simeq 0.0085\mathcal{L}_{L,\nu,c}$ is nearly but not quitely counterbalanced by its negative gravitational angular momentum luminosity $\mathcal{L}_{L,g} \simeq -0.0075\mathcal{L}_{L,\nu,c}$. That $\mathcal{L}_{L,\nu}$ and $\mathcal{L}_{L,g}$ are both offset slightly from zero also tells us that ringlet self-gravity causes the streamline's shape and/or orientations differ slightly from the non-gravitating solution of Borderies et al. (1982). Interestingly, Fig. 12 also shows that $\mathcal{L}_{L,\nu} + \mathcal{L}_{L,g}$ does not sum precisely to zero, $i.e.$ $\mathcal{L}_L = \mathcal{L}_{L,\nu} + \mathcal{L}_{L,g} \simeq 0.001\mathcal{L}_{L,\nu,c}$, yet Section 5.4 will show that this ringlet's energy luminosity $\mathcal{L}_E$ is zero. Evidently it is $\mathcal{L}_E$ that must be zero (rather than $\mathcal{L}_L$) in order for a viscous gravitating ringlet to be self-confining,

Figure 9. The nominal ringlet's angular shear $\partial\omega/\partial r$ is plotted versus relative longitude φ at selected moments in time; this quantity is negative when the inner streamline has the higher angular speed $\omega = v_\theta/r$. When the simulation starts, this nearly circular ringlet has eccentricity gradient $e' = 0$, so $\partial\omega/\partial r \simeq -3\Omega/2r \simeq -1.5$ when evaluated natural units (blue curve). The ringlet's e' then grows over time (orange, green, red curves), which reverses the sign of $\partial\omega/\partial r$ near periapse when $e' > 0.75$; here the inner ringlet's angular speed is slower than the outer ringlet, and viscous friction causes angular momentum to instead flow inwards at these longitudes.

since $\mathcal{L}_E = 0$ is required for the streamlines' semimajor axes a to not evolve relative to each other. That this ringlet's $\mathcal{L}_L$ is slightly nonzero while $\mathcal{L}_E = 0$ also implies that this ringlet's eccentricities are still slowly evolving despite the self-confinement, which is evident in inset Fig. 13.

5.4. *gravitational transport*

The ringlet's viscous $\mathcal{F}_{L,\nu}$ and gravitational $\mathcal{F}_{L,g}$ angular momentum fluxes are shown Fig. 14. That Figure shows how viscous friction tends to transport angular momentum radially inwards, $\mathcal{F}_{L,\nu}(\varphi) < 0$, at longitudes nearer periapse where $|\varphi| \sim 0$, and outwards at all other longitudes, with that flux reversal being due to the reversal of the ringlet's angular velocity gradient (Fig. 9). Figure 14 also shows that the ringlet's gravitational transport of angular momentum is inwards as ring-matter approaches periapse where $\varphi < 0$, and is outwards $\mathcal{F}_{L,g}(\varphi) > 0$ post-periapse, with that asymmetry being due to the ringlet's negative periapse twist, $\tilde{\omega}' < 0$ (Fig. 8).

Figure 15 shows the ringlet's viscous $\mathcal{L}_{E,\nu}$ and gravitational luminosity $\mathcal{L}_{E,g}$ over time. That Figure's gravitational angular momentum luminosity is computed via

$$\mathcal{L}_{E,g}(a) = \oint \mathcal{F}_{E,g}(\varphi)r\,d\varphi = \oint \lambda r \mathbf{A}_g^1 \cdot \mathbf{v}\,d\varphi \qquad (17)$$

where $\mathbf{A}_g^1$ is the one-sided gravitational acceleration experienced by a particle in streamline a. Note that even though $\mathcal{F}_{E,\nu}$ and $\mathcal{F}_{E,g}$ have very different spatial dependances, the influence of viscosity and

Figure 10. The nominal ringlet's viscous angular momentum flux $\mathcal{F}_{L,\nu}(\varphi)$, Eqn. (15), is plotted versus ringlet relative longitude $\varphi = \theta - \tilde{\omega}$ about the ringlet's inner streamline at selected times t/τ_ν, with the ringlet's eccentricy gradient e' also indicated, and $\mathcal{F}_{L,\nu,c}$ the angular momentum flux in a circular ringlet

Figure 11. Nominal ringlet's viscous angular momentum luminosity $\mathcal{L}_{L,\nu}$ (blue curve) versus time t/τ_ν and in units of a circular ring's viscous angular momentum luminosity $\mathcal{L}_{L,\nu,c}$, as well as the ringlet gravitational angular momentum luminosity $\mathcal{L}_{L,g}$ (orange curve).
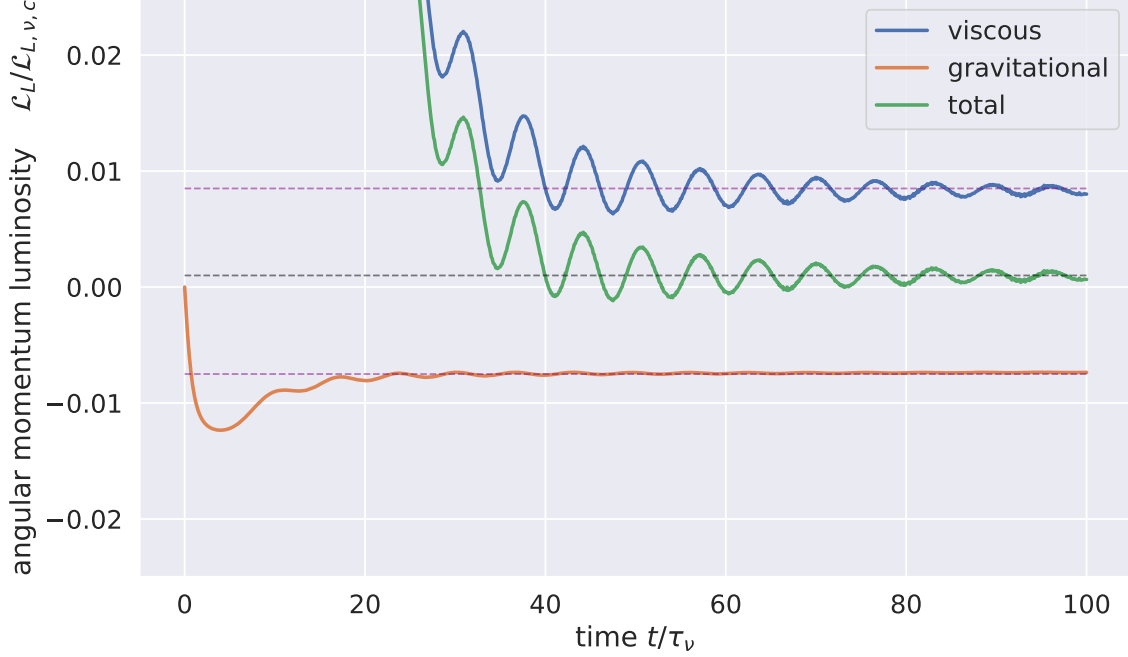
Figure 12. Figure 11 is replotted to highlight that the ringlet's viscous angular momentum luminosity $\mathcal{L}_{L,\nu}$ (blue curve) always stays positive (indicating that the viscous transport of angular momentum is radially outwards) which is nearly but not entirely balanced by the ringlet's negative (*i.e.* inwards) gravitational angular momentum luminosity $\mathcal{L}_{L,g}$ (orange) after time $t \gg 35\tau_\nu$. Green curve is total angular momentum luminosity $\mathcal{L}_{L,\nu} + \mathcal{L}_{L,g} \simeq 0.001\mathcal{L}_{L,\nu,c}$.

gravity still conspire to sum to zero in the orbit-integrated sense such that $\mathcal{L}_E = \oint(\mathcal{F}_{E,\nu} + \mathcal{F}_{E,g})r d\varphi = 0$ after the ringlet has settled into the self-confining state.

Note that Fig. 15 also shows that the ringlet's gravitational energy luminosity is zero. Which is to be expected since the streamlines' gravitating ellipses only interact via their secular perturbations, and secular perturbations do no work (Brouwer & Clemence 1961), hence $\mathcal{L}_{E,g} = 0$.

5.5. *variations*

Simulation survey...

6. ACKNOWLEDGMENTS

APPENDIX

A. APPENDIX A

Derive the more accurate drift step used by epi_int_lite...

B. APPENDIX B
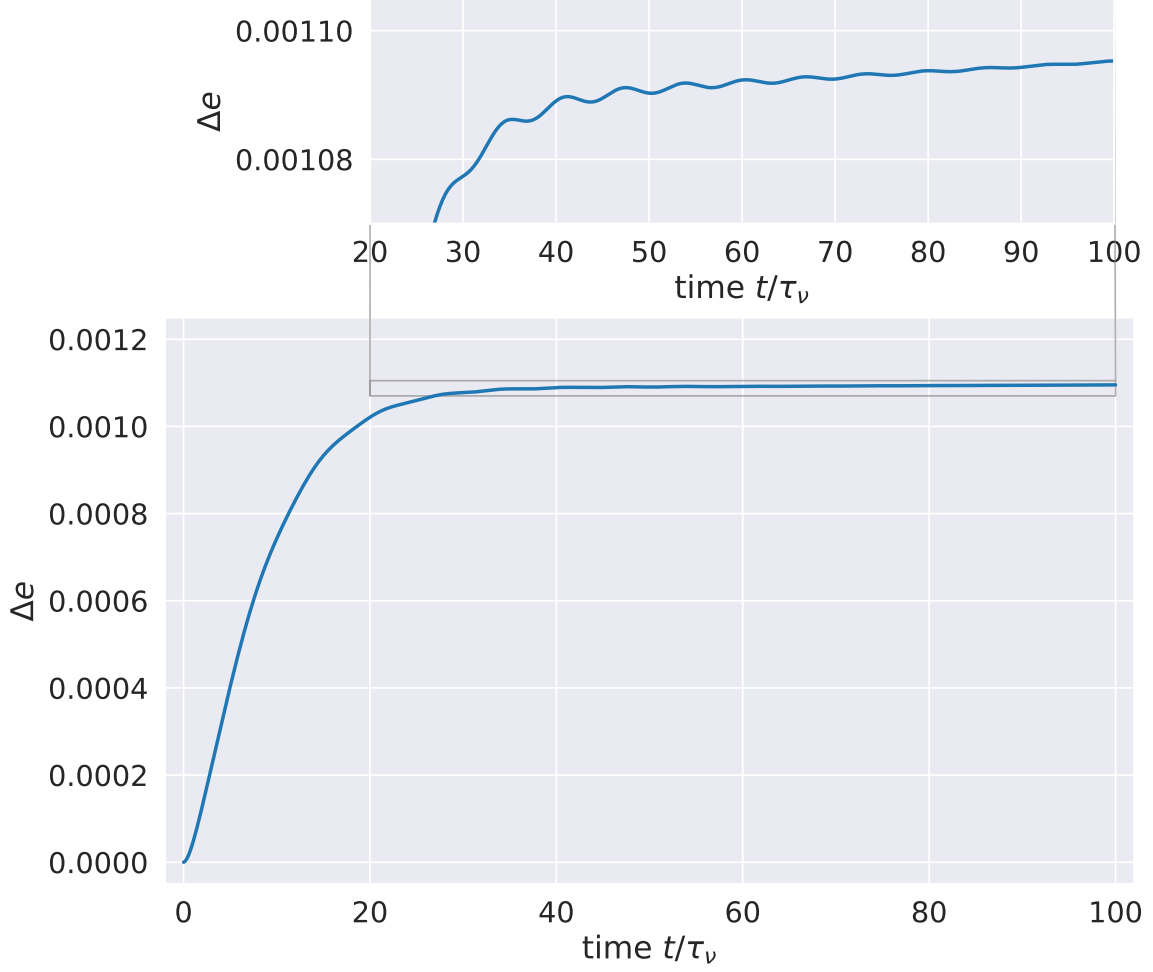
Compare epi_int_lite to theoretical predictions

Figure 13. The nominal ringlet's eccentricity difference $\Delta e = e_{\mathrm{outer}} - e_{\mathrm{inner}}$ from Fig. 4, with inset plot showing that Δe continues to slowly grow even after self-confinement is established.

C. APPENDIX D

This examines the viscous evolution of a narrow eccentric non-gravitating ringlet that is identical to the nominal ringlet of Section 4.1 but with ringlet self-gravity neglected and $J_2 = 0$. As the orange curve in Fig. 17 shows, the non-gravitating ringlet's radial width Δa grows steadily over time due to ringlet viscosity, long after the nominal self-gravitating ringlet (blue curve) has settled into the self-confining state by time $t \sim 15\tau_\nu$. This is due to the ringlet's secular gravitational perturbations of itself, which tends to excites the ringlet's outer streamline's eccentricity at the expense of the inner streamline (see Fig. 3) until the ringlet eccentricity gradient e' (blue curve in Fig. 18) grows beyond the limit required for complete angular momentum flux reversal that results in the ringlet's radial confinement (dotted line). Note that viscosity also excites the non-gravitating ringlet's eccentricity gradient some (orange curve), but not sufficiently to halt the ringlet's viscous spreading.

D. APPENDIX E

This Appendix will use the orbit elements derived in Appendix A to derive Eqn. 15 from 14, and then Eqn. (16).
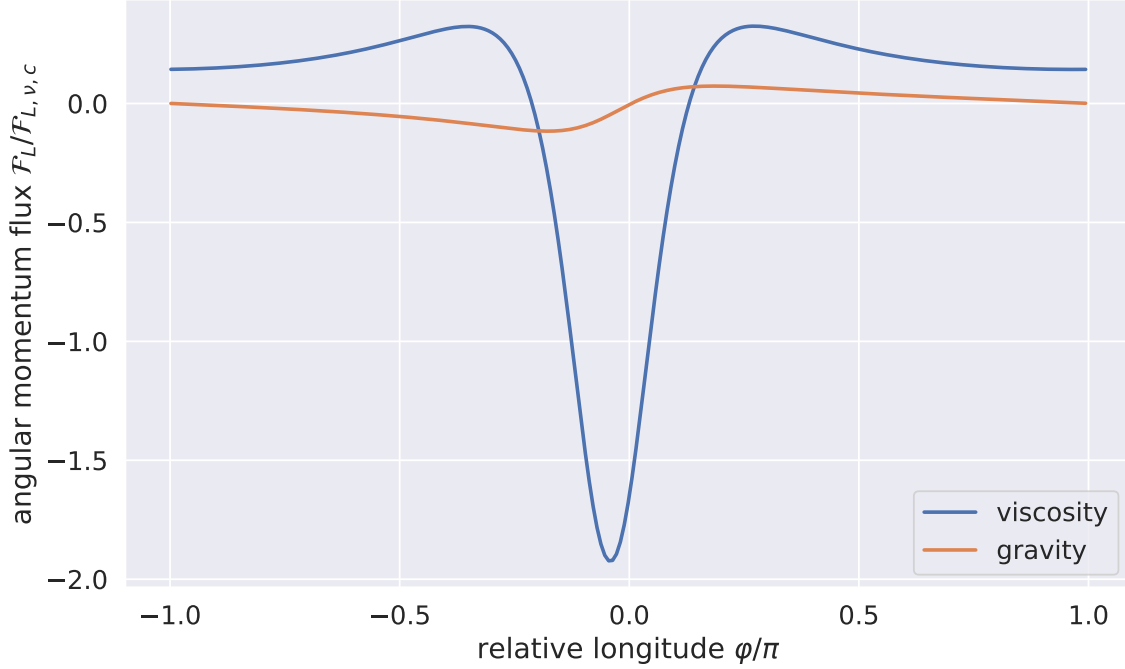
Figure 14.   The nominal ringlet's viscous angular momentum flux $\mathcal{F}_{L,\nu}(\varphi)$ (blue curve) is computed via Eqn. (14) and plotted in units of a circular ringlet's flux $\mathcal{F}_{L,\nu,c}$ and versus relative longitude φ as the simulation's end at time $t = 100\tau_\nu$, as well as the ringlet's gravitational angular momentum flux $\mathcal{F}_{L,g}(\varphi)$ (orange curve via Eqn. 10).

E. APPENDIX F

Viscous and gravitational energy transport...

REFERENCES

Borderies, N., Goldreich, P., & Tremaine, S. 1982, Nature, 299, 209

—. 1983, Icarus, 55, 124

—. 1985, Icarus, 63, 406

Brouwer, D., & Clemence, G. M. 1961, Methods of celestial mechanics (New York: Academic Press, 1961)

Chambers, J. E. 1999, MNRAS, 304, 793

Goldreich, P., & Tremaine, S. 1979, AJ, 84, 1638

Hahn, J. M., & Spitale, J. N. 2013, ApJ, 772, 122

Pringle, J. E. 1981, ARA&A, 19, 137

Rimlinger, T., Hamilton, D., & Hahn, J. M. 2016, in AAS/Division of Dynamical Astronomy Meeting, Vol. 47, AAS/Division of Dynamical Astronomy Meeting, #47, id.400.02
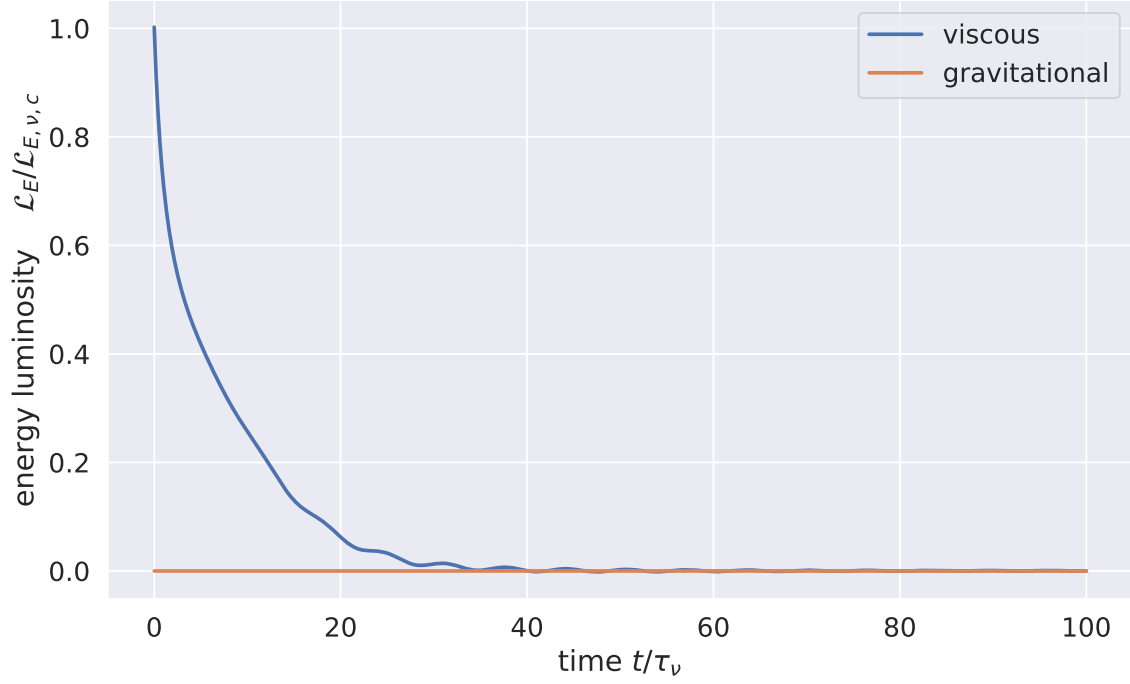
Figure 15. Nominal ringlet's viscous energy luminosity $\mathcal{L}_{E,\nu}$ (blue curve) versus time t/τ_ν and in units of a circular ring's viscous energy luminosity $\mathcal{L}_{E,\nu,c}$, as well as the ringlet gravitational energy luminosity $\mathcal{L}_{E,g}$ (orange curve).
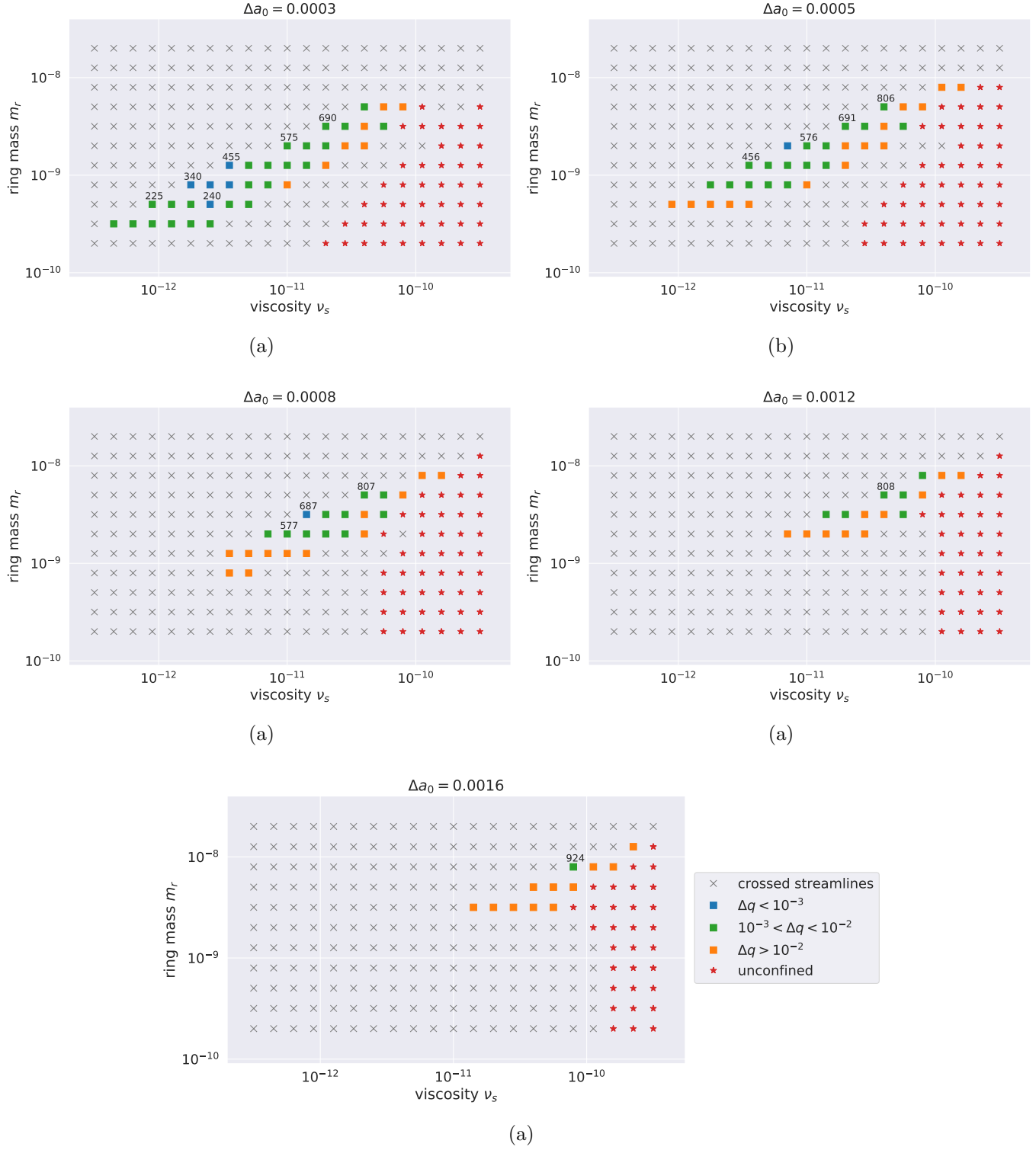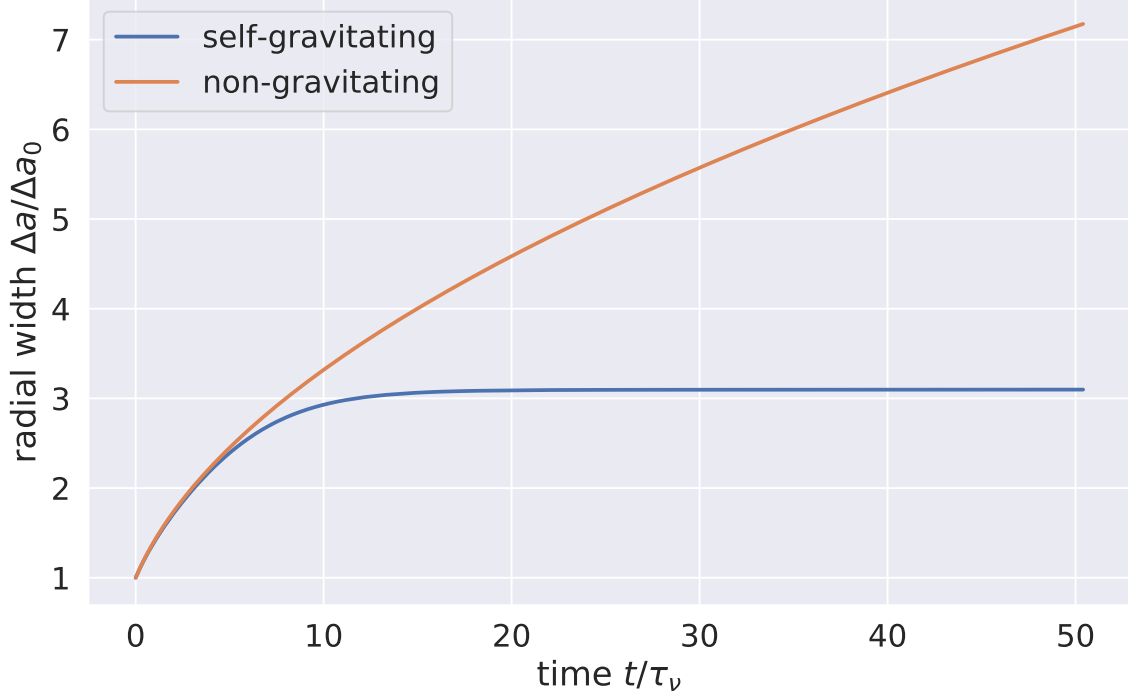
Figure 16. caption...

Figure 17. Blue curve is the nominal ringlet's semimajor axis width Δa versus time t, and this ringlet's radial spreading ceases by time $t \sim 15\tau_\nu$ when it's self-gravity has excited the ringlet's eccentricity gradient e' sufficiently; see blue curve in Fig. 18. Orange curve shows that the non-gravitating ringlet's Δa grows without limit due to the ringlet's much lower eccentricity gradient. Note that planetary oblateness would cause the non-gravitating streamlines to precess differentially and eventually cross when $J_s > 0$, so the non-gravitating simulation also sets $J_2 = 0$ to avoid differential precession.
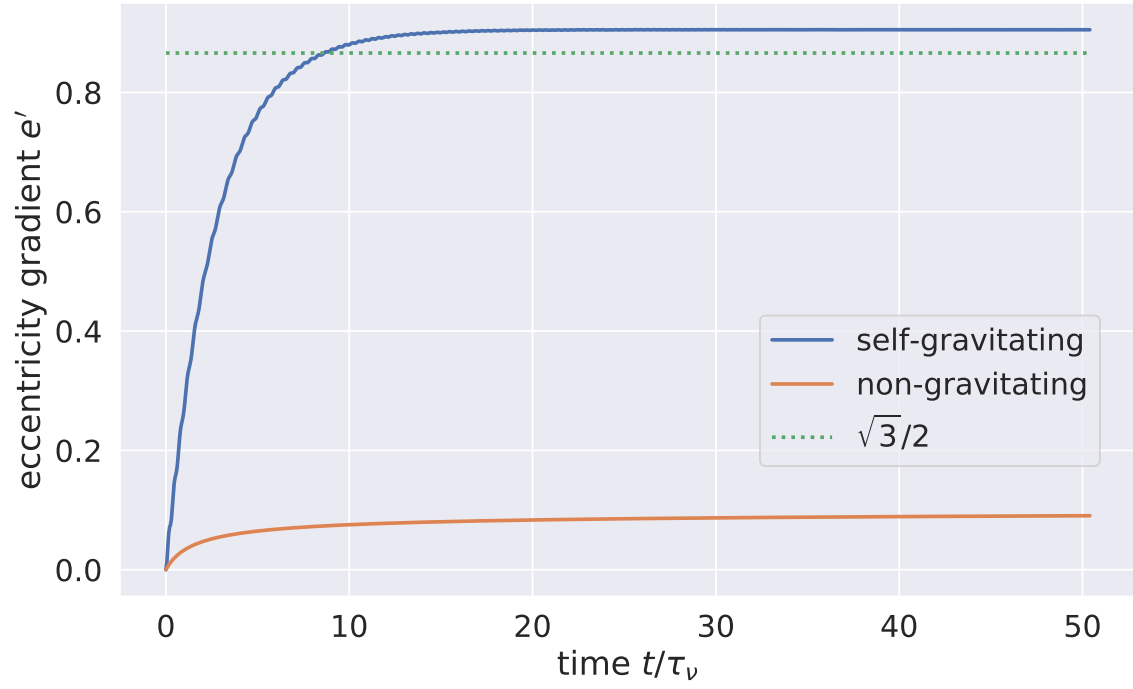
Figure 18. blah